Coevolution of dust and chemistry in galaxy simulations with a resolved interstellar medium

Hu, C.Y.; Sternberg, A.; Dishoeck, E.F. van

The Astrophysical Journal, 952:140 (14pp), 2023 August 1 https://doi.org/10.3847/1538-4357/acdcfa

Coevolution of Dust and Chemistry in Galaxy Simulations with a Resolved Interstellar Medium

Chia-Yu Hu (胡家瑜)[1,2], Amiel Sternberg[1,3,4], and Ewine F. van Dishoeck[1,5]
[1] Max-Planck-Institut für Extraterrestrische Physik, Giessenbachstrasse 1, D-85748 Garching, Germany; cyhu.astro@gmail.com
[2] Department of Astronomy, University of Florida, 211 Bryant Space Science Center, Gainesville, FL 32611, USA
[3] School of Physics & Astronomy, Tel Aviv University, Ramat Aviv 69978, Israel
[4] Center for Computational Astrophysics, Flatiron Institute, 162 5th Avenue, New York, NY 10010, USA
[5] Leiden Observatory, Leiden University, P.O. Box 9513, NL-2300 RA Leiden, The Netherlands
Received 2023 January 12; revised 2023 May 26; accepted 2023 June 7; published 2023 July 25

Abstract

Nearby dwarf irregular galaxies are ideal laboratories for studying the interstellar medium (ISM) at low metallicity, which is expected to be common for galaxies at very high redshift being observed by JWST. We present the first high-resolution (∼0.2 pc) hydrodynamical simulations of an isolated low-metallicity ($0.1\,Z_{\odot}$) dwarf galaxy coupled with a time-dependent chemistry network and a dust evolution model where dust is locally produced and destroyed by various processes. To accurately model carbon monoxide (CO), we post-process the simulations with a detailed chemistry network including the time-dependent effect of molecular hydrogen (H_2). Our model successfully reproduces the observed star formation rate and CO(1–0) luminosity (L_{CO}). We find that dust growth in dense gas is required to reproduce the observed L_{CO} otherwise CO would be completely photodissociated. In contrast, the H_2 abundance is extremely small and is insensitive to dust growth, leading to a CO-to-H_2 conversion factor that is only slightly higher than the Milky Way value despite the low metallicity. An observationally inferred dust-to-gas ratio is thus underestimated if adopting the metallicity-dependent CO-to-H_2 conversion factor. The newly produced dust in dense gas mixes with the ISM through supernova feedback without being completely destroyed by sputtering, which leads to galactic outflows 20%–50% dustier than the ISM, providing a possible source for intergalactic dust.

Unified Astronomy Thesaurus concepts: Interstellar medium (847); Astrochemistry (75); Hydrodynamical simulations (767)

1. Introduction

The formation and evolution of galaxies are critically controlled by how stars form and how they affect the gas cycle in and around galaxies via stellar feedback (Somerville & Davé 2015; Naab & Ostriker 2017). Over the last decade, the cold, star-forming gas (dominated by molecular hydrogen, H_2) in galaxies from the local universe to *cosmic noon* at redshift $z \sim 2$ has been systematically quantified by submillimeter and far-infrared (FIR) telescopes, leading to a physical picture where galaxies grow primarily by gas accretion onto the rotationally supported disks, which fuels star formation in their interstellar medium (ISM) regulated by feedback across cosmic time (see Tacconi et al. 2020 and references therein). The molecular gas mass inferred by dust-based methods is broadly consistent with the conventional method based on carbon monoxide (CO), strengthening the robustness of the results.

However, while significant progress has been made in understanding the evolution of star-forming gas in galaxies of solar or slightly subsolar metallicity, little is known about the ISM of low-metallicity galaxies ($Z \lesssim 0.1Z_{\odot}$). In the era of the James Webb Space Telescope (JWST), a deep understanding of ISM chemistry at low metallicity is urgently needed as we begin to observe galaxies in the very early universe. Indeed, Curtis-Lake et al. (2022) recently reported four galaxies at extremely high redshift ($z \sim 10$–13) discovered by JWST, all of which have metallicity of $Z < 0.1Z_{\odot}$.

On the other hand, nearby dwarf irregular galaxies provide a unique laboratory to study the chemical properties and observational signatures of the star-forming gas at comparably low metallicity in great detail thanks to their proximity, even though their galaxy properties (such as mass, size, surface density, etc.) may be different from their high-redshift counterparts. It has long been recognized that CO emission in these galaxies tends to be extremely faint and becomes undetected when the metallicity drops below $0.2Z_{\odot}$ (Leroy et al. 2005; Schruba et al. 2012; Madden et al. 2020). This has changed with the advent of the Atacama Large Millimeter/submillimeter Array (ALMA) thanks to its extremely high sensitivity. Rubio et al. (2015) observed the Wolf–Lundmark–Melotte (WLM) dwarf galaxy and detected the first CO emission at a metallicity of $0.1Z_{\odot}$. However, the molecular gas mass still cannot be robustly determined due to the highly uncertain CO-to-H_2 conversion factor. Similarly, the dust-based method suffers from the uncertainty in the assumed dust-to-gas ratio (DGR) that has been shown to scale superlinearly with metallicity in this regime, but the exact scaling relation is still uncertain (see, e.g., Rémy-Ruyer et al. 2014; De Vis et al. 2019). In fact, the detection of CO in the WLM galaxy is rather surprising given the extremely low DGR expected at this metallicity.

Recent hydrodynamical simulations coupled with time-dependent chemistry have achieved the required numerical resolution of a few parsecs to directly resolve feedback from individual supernova (SN) explosions in isolated dwarf

galaxies (Hu et al. 2016, 2017; Emerick et al. 2019; Hu 2019; Lahén et al. 2020, 2023; Hislop et al. 2022; Katz et al. 2022; Steinwandel et al. 2022a, 2022b; Whitworth et al. 2022, 2023). This is an important milestone as it avoids the need for sub-grid prescriptions for SN feedback one of the major uncertainties in cosmological simulations. Coincidentally, H_2 can be resolved at a similar resolution (Gong et al. 2018), at least at solar metallicity. However, proper modeling of CO requires a significantly higher resolution of $\sim$0.1 pc (Seifried et al. 2017; Hu et al. 2021) as CO typically exists in dense, spatially compact gas. Lagrangian codes are therefore particularly suitable for such a task thanks to their built-in adaptive spatial resolution that can more easily reach sub-parsec scales. Meanwhile, the carbon network responsible for CO formation is much larger than the hydrogen network (Sternberg & Dalgarno 1995), leading to a significant computational overhead if coupled with simulations, compromising the achievable resolution. To address this dilemma, Hu et al. (2021) introduced a hybrid approach where the hydrogen network is solved on the fly to capture the time-dependent (nonsteady-state) effect of H_2 while an accurate chemistry network including carbon chemistry is solved in post-processing.

Dust plays an important role in ISM chemistry. The surfaces of dust grains are the main sites where H_2 formation occurs, which then initiates the formation of other important molecules such as CO. Furthermore, dust provides shielding against the Lyman–Werner radiation that can photodissociate both H_2 and CO. Observations of the Small and Large Magellanic Clouds (SMC and LMC) have demonstrated that the spatially resolved DGR can vary by almost an order of magnitude from region to region in low-metallicity galaxies, indicating significant dust evolution (Roman-Duval et al. 2017, 2022). However, simulations that resolve the ISM to date have all assumed a constant DGR in both space and time, which is an oversimplification.

Cosmological simulations and isolated galaxy simulations with comparable resolution have started to include dust evolution models at different levels of sophistication (Aoyama et al. 2017, 2018; McKinnon et al. 2017, 2018; Li et al. 2019; Lewis et al. 2022; Lower et al. 2023; Parente et al. 2022; Romano et al. 2022). However, these simulations do not resolve either SN feedback or the density structure of the ISM, forcing them to adopt dust evolution models in a sub-grid fashion. For example, dust destruction by supernovae (SNe) is generally based on results from 1D calculations in plane-parallel shocks, which does not apply to more complex situations such as an inhomogeneous ISM or clustered SNe. While this simplification is perhaps justified as SN feedback in these simulations is unresolved anyway, a more accurate model is clearly desirable in resolved simulations. Hu et al. (2019) introduced a numerical method to directly simulate thermal and nonthermal sputtering of dust designed for simulations with parsec or sub-parsec resolutions. However, the model did not include any dust production processes, nor was it coupled with chemistry.

In this work, we extend the dust evolution model in Hu et al. (2019) by including dust growth in cold gas and dust production in asymptotic giant branch (AGB) stars. We couple this with the time-dependent chemistry network and the ISM model developed by Hu et al. (2016, 2017, 2021) and perform hydrodynamical simulations of an isolated dwarf galaxy similar to the WLM galaxy at a mass resolution of 1 $M_\odot$ (spatial resolution $\sim$0.2 pc). To our knowledge, this is the first ISM-resolved simulation coupled with chemistry and dust evolution (but see Romano et al. 2022 for a model of significantly coarser resolutions). This paper is organized as follows. In Section 2, we describe our numerical model. In Section 3, we study how dust evolution affects the ISM chemistry, how the DGR is distributed in the ISM and galactic outflows, and how the projected DGR varies with the gas surface density at different telescope beam sizes. In Section 4, we discuss the implications of our results for the observationally inferred DGR and the intergalactic dust. In Section 5, we summarize our work.

2. Numerical Methods

2.1. Gravity and Hydrodynamics

We use the public version of GIZMO (Hopkins 2015), a multi-solver code for hydrodynamics that is built on the massively parallel TreeSPH code GADGET-3 (Springel 2005). We adopt its meshless finite-mass (MFM) solver for hydrodynamics (Hopkins 2015), which is a variation of the meshless Godunov method (Gaburov & Nitadori 2011). Gravity is calculated using the Barnes–Hut method (`treecode`).

2.2. The ISM Model

In this section, we summarize the physical processes in the ISM in our simulations excluding dust evolution, which are described in Section 2.3. The methods and implementations are largely based on Hu et al. (2016, 2017, 2021) where more details can be found.

2.2.1. Time-dependent Cooling and Chemistry

We adopt a time-dependent chemistry network developed in Glover & Mac Low (2007) and Glover & Clark (2012a) that is widely used in ISM simulations. The abundances of H_2, H^+, H I, and the free electron fraction are integrated based on the chemical reactions in the network. The hydrogen network includes H_2 formation on dust, H_2 destruction by photodissociation, collisional dissociation, and cosmic-ray ionization, and recombination in the gas phase and on dust grains. Individual cooling and heating processes are calculated based on the time-dependent chemical abundances, which include cooling from fine structure metal lines, molecular lines, Lyα, H_2 collisional dissociation, collisional ionization of H, and recombination of H^+ in the gas phase and on grains. Heating includes a photoelectric effect, cosmic-ray ionization, H_2 photodissociation, UV pumping of H_2, and the formation of H_2. Following Clark et al. (2012), shielding against far-UV (FUV) radiation uses the HEALPIX algorithm (Górski & Hivon 2011) in combination with the `treecode` approximation to integrate the relevant column densities along 12 sightlines up to a predefined radius of 100 pc. Self-shielding of H_2 follows the fitting formula from Draine & Bertoldi (1996) [6] using the H_2 column densities obtained by the HEALPIX method and the Doppler factor b from gas temperature. We neglect turbulent broadening that could reduce self-shielding. However, the Doppler factor b mainly affects self-shielding where the H_2 column density is less than 10^{16} cm^{-2}, which is a very thin layer we do not resolve. We adopt a constant cosmic ray ionization rate of H I

[6] We do not adopt the improved fitting formula in Wolcott-Green et al. (2011) as most of the H_2 forms in low temperatures where the fitting formula from Draine & Bertoldi (1996) is a reasonable approximation.

$\zeta_{\rm CR} = 10^{-17}{\rm s}^{-1}$, an order of magnitude lower than that observed in the Milky Way (Indriolo et al. 2015) to account for the low star formation rate (SFR) in our simulated galaxy. The FUV radiation field is directly calculated from star particles (see Section 2.2.5).

2.2.2. Star Formation

We adopt the stochastic star formation recipe commonly used in the field of galaxy formation. A gas particle eligible for star formation is converted into a star particle of the same mass on a timescale of $t_{\rm ff}/\epsilon_{\rm sf}$ stochastically, where $\epsilon_{\rm sf}$ is the star formation efficiency and $t_{\rm ff} = \sqrt{3\pi/(32G\rho)}$ is the gas freefall time where G is the gravitational constant and ρ is the gas density. We adopt $\epsilon_{\rm sf} = 0.5$ in this work. Such high efficiency is justified by our resolution as we can follow the gravitational collapse down to the scales of individual molecular cores. Gas is eligible for star formation when its local Jeans mass $M_{\rm J} = (\pi^{2.5}c_s^3)/(6G^{1.5}\rho^{0.5})$, drops below the kernel mass $M_{\rm ker} = N_{\rm ngb}m_{\rm g}$, where c_s is the speed of sound, $m_{\rm g}$ is the gas-particle mass, and $N_{\rm ngb} = 32$ is the number of neighboring particles in a kernel.

2.2.3. Sampling Individual Stars from an IMF

Massive stars (initial mass $>8\,M_\odot$) inject energy and momentum into their surrounding gas commonly termed as *stellar feedback*. At our resolution of 1 $M_\odot$ per star particle, it is unphysical to assume that each particle represents a star cluster with a fully sampled stellar initial mass function (IMF), as is commonly the case in cosmological simulations with much coarser resolutions. Following Hu et al. (2021), we adopt the technique of *importance sampling* to stochastically sample stellar masses from a Kroupa IMF (Kroupa 2001). The sampled stellar masses are used to determine the stellar lifetime (Ekström et al. 2012) and UV luminosity from the BaSeL stellar library (Lejeune et al. 1997, 1998) This does not affect the dynamics, as the gravitational masses of star particles (m_*) remain unchanged.

2.2.4. Stellar Feedback

We include stellar feedback from SNe and photoionization. SN feedback is done by injecting thermal energy of 10^{51} erg per SN into its nearest $N_{\rm ngb}$ gas particles in a kernel-weighted fashion. As our resolution is able to resolve the Sedov–Taylor phase in each SN event, a simple thermal feedback is able to achieve numerical convergence (Hu 2019). Feedback from photoionization follows that used in Hu et al. (2017), where each massive star searches for its ionization front iteratively by balancing recombination and photoionization and heats up the interior gas to 10^4 K. The hydrogen is assumed to be fully ionized in the H II regions where chemistry is turned off. This approach reproduces the dynamics of an expanding H II region predicted by radiative transfer codes in a uniform medium. More importantly, it captures the correct behaviors in overlapping H II regions where a naive Strömgren-sphere method would suffer from the numerical artifact of double counting.

2.2.5. Spatially Variable FUV Radiation

Following Hu et al. (2017), the unattenuated FUV radiation field is both spatially and temporally variable and is calculated directly from the star particles. For a given gas particle, every star particle contributes a radiation flux of $L_{\rm FUV}/(4\pi r^2)$ where $L_{\rm FUV}$ is the FUV luminosity based on the sampled stellar mass and r is the distance between the gas and star particle. The summation is over all star particles and is done via the `treecode` approximation to avoid the $O(n^2)$ operation and speed up the calculation. The FUV radiation affects both the thermal balance via photoelectric heating and the chemistry via photodissociation.

2.3. Dust Evolution Model

We adopt the *one-fluid* approach where dust is assumed to be spatially coupled with the gas. This is justified as dust is expected to be charged and gyrates around the magnetic fields in the ISM with a small gyro-radius. Each gas particle is associated with a dust mass $m_d = m_d({\rm Sil}) + m_d({\rm C})$, where m_d(Sil) and m_d(C) are, respectively, the masses of silicate dust and carbonaceous dust, which evolve separately in the simulations due to the production and destruction processes as we describe below. Dust grains are assumed to be spherical with a radius of a and a material density of s_d, which leads to a grain mass of $m_{\rm gr} = (4\pi a^3/3)s_d$. The formation or destruction rate of dust can be expressed as

$$\frac{dm_d}{dt} = N_{\rm gr}\frac{dm_{\rm gr}}{dt} = 3\frac{\dot{a}}{a}m_d, \tag{1}$$

where $N_{\rm gr} = m_d/m_{\rm gr}$ is the number of dust grains in a gas cell. Time integration is done via sub-cycling in order to resolve the timescales of dust dynamics and sputtering that can be orders of magnitude smaller than the hydrodynamical time steps.

We include physical processes that directly modify m_d: sputtering, dust growth, and dust formation in AGB ejecta. Processes that modify the grain size while keeping m_d fixed, such as shattering and coagulation, are not included. This is because we are only interested in the evolution of dust mass rather than other dust properties such as the extinction law. We adopt a fixed grain-size distribution that follows Mathis et al. (1977) (the *MRN* distribution).

2.3.1. Sputtering

In shocks or in hot gas, dust can be destroyed via sputtering, which returns metals locked up in dust grains back to the ISM. We adopt the sputtering model in Hu et al. (2019), which includes thermal and nonthermal sputtering, which we briefly summarize as follows. The dust destruction rate due to sputtering can be expressed as

$$\left.\frac{dm_d}{dt}\right|_{\rm sput} = -\frac{m_d}{t_{\rm sput}}, \tag{2}$$

where

$$t_{\rm sput} \equiv \frac{a}{3nY_{\rm tot}} = 10\ {\rm kyr}\left(\frac{a}{0.03\mu{\rm m}}\right)\left(\frac{n}{{\rm cm}^{-3}}\right)^{-1}\left(\frac{10^6\ Y_{\rm tot}}{\mu{\rm m\ yr}^{-1}{\rm cm}^3}\right)^{-1}, \tag{3}$$

where n is the hydrogen number density and $Y_{\rm tot}$ is the erosion rate that includes thermal and nonthermal sputtering, which we adopt from Nozawa et al. (2006). The thermal erosion rate is a function of gas temperature while the nonthermal erosion rate is a function of the relative bulk velocity between dust and gas,

which we obtain by integrating the equation of motion for dust accounting for direct collision, plasma drag, and betatron acceleration.

2.3.2. Dust Growth

Dust can grow in cold gas when gas-phase metals interact with dust and stick to the surfaces of dust grains, which can be viewed as the reverse process of sputtering. The exact mechanism is still poorly understood, though its feasibility has been supported by laboratory experiments (Krasnokutski et al. 2014; Henning et al. 2018; Rouillé et al. 2020). The dust production rate due to dust growth can be expressed as

$$\left.\frac{dm_d}{dt}\right|_{\rm grow} = (1-f)\frac{m_d}{t_{\rm grow}}, \tag{4}$$

where $t_{\rm grow}$ is the dust growth timescale (see below) and f is the fraction of metals locked in dust grains. For element A (where $A =$ Si or C), this can be written as

$$f_A = \frac{m_{A,\rm d}}{m_{A,\rm tot}} = \frac{m_d(A)\xi_A}{m_{\rm g}X_A Z'}, \tag{5}$$

where $m_{\rm A,d}$ is the mass of element A in the dust phase, $m_{\rm A,tot}$ is the total mass of element A (dust + gas), $X_{\rm A}$ is the solar abundance of element A, and $\xi_{\rm A}$ is the mass fraction of element A in the assumed grain material. For carbonaceous dust, $\xi_{\rm C} = 1$. For silicate dust, we adopt $MgFeSiO_4$ as the grain material, which leads to $\xi_{\rm Si} = 0.165$. The dust growth timescale takes the following form:

$$t_{\rm grow} = 1.5\ {\rm Gyr}\left(\frac{n}{\rm cm^{-3}}\right)^{-1}\left(\frac{T}{100{\rm K}}\right)^{-0.5} \times \left(\frac{a_3}{0.03\mu{\rm m}}\right)(Z'\alpha_s D_{\rm eff})^{-1}. \tag{6}$$

Here, α_s is the sticking coefficient, $a_3 \equiv \langle a^3\rangle/\langle a^2\rangle$ is the average grain size where the bracket $\langle\ldots\rangle$ refers to integration over the grain size distribution, and $D_{\rm eff} \equiv \langle a^2 D(a)\rangle/\langle a^2\rangle$ is the enhancement factor $D(a)$ due to Coulomb focusing (Weingartner & Draine 1999) weighted by the surface area of grains. The sticking coefficient encompasses the complex physical and chemical processes on the surfaces of grains, which is still uncertain (see, e.g., Zhukovska et al. 2018 for a discussion). To first order, it is expected to be close to unity at low temperatures and decrease substantially at high temperatures. We follow Zhukovska et al. (2016) and assume that $\alpha_s = 1$ at $T < 300$ K while $\alpha_s = 0$ at $T \geqslant 300$ K. The area-weighted enhancement factor $D_{\rm eff}$ is also uncertain and is expected to depend on a number of properties such as density, temperature, free electron fraction, grain-size distribution, and grain charge. Weingartner & Draine (1999) found that Coulomb focusing shortens the growth timescale by more than an order of magnitude. However, Priestley et al. (2021) found a much weaker effect if the evolution of grain size is taken into account. We adopt $D_{\rm eff} = 10$ for simplicity, but the uncertainties in both α_s and $D_{\rm eff}$ are potential caveats of our model.

2.3.3. Dust Production from AGB Stars

We adopt the mass-dependent dust yields from Zhukovska et al. (2008) at $Z' = 0.1$ based on the individual stellar masses sampled from the IMF to account for dust produced in the ejecta of AGB stars. The produced dust mass is injected into the neighboring gas particles in a kernel-weighted fashion. We do so only for carbonaceous dust as the silicate dust yields at this metallicity is essentially zero. Dust produced from AGB stars is expected to have a subdominant effect on the spatial variation of the DGR as AGB stars are more uniformly distributed in the ISM compared to sputtering in SN shocks and dust growth in dense clouds that are highly clustered.

2.4. Chemistry Network in Post-processing

In order to accurately model the transitions of C^+/C I/CO (the *carbon cycle*), a detailed carbon chemistry is required, which is much more complicated and computationally costly to solve compared to the hydrogen chemistry. We therefore post-process the simulation snapshots using `ASTROCHEMISTRY`,[7] a chemistry network code developed in Hu et al. (2021). It consists of 31 species: H, H^-, H_2, H^+, H_2^+, H_3^+, e^-, He, He^+, HeH^+, C, C^+, CO, HCO^+, O, O^+, OH, OH^+, H_2O^+, H_3O^+, H_2O, O_2, CO^+, O_2^+, CH_2, CH_2^+, CH, CH^+, CH_3^+, Si^+, and Si. All chemical reactions in the UMIST database (McElroy et al. 2013) that exclusively involve the abovementioned species are included in the network, which leads to 286 reactions in total. The time-dependent abundances of H_2 and H^+ in the simulations are taken as input parameters when solving the network. This is crucial as H_2 can be out of steady state significantly, especially at low metallicity. The free electron abundance is calculated from charge conservation, which is dominated by H^+ in the diffuse ISM and by C^+ in the dense gas. Both dust shielding and gas shielding (including H_2 and CO) for CO are included using a `HealPIX` method similar to the time-dependent chemistry.[8] This approach has been applied to ISM-patch simulations that successfully reproduced the observed relationship between the column densities of CO and H_2 in galactic clouds (Hu et al. 2021) as well as the Milky Way CO-to-H_2 conversion factor ($X_{\rm CO}$) (Hu et al. 2022). We do not include the effect of dust depletion in post-processing and instead assume constant gas-phase metal abundances. The significance of depletion depends on the competition between dust growth and CO formation that requires time-dependent carbon chemistry, which is an interesting topic for future work.

Hu et al. (2022) found that CO(1–0) is almost always optically thin in their simulated ISM at $Z' = 0.1$. This is primarily a direct consequence of the low CO abundance. Furthermore, CO(1–0) can remain optically thin even at the highest column densities as the population of CO is distributed over more excited levels. Assuming optically thin conditions, the CO luminosity from each gas particle can be expressed by

$$l_{\rm CO} = 0.5\lambda_{10}^3 T_{10} A_{10} n_{\rm CO} f_1 \overline{V}, \tag{7}$$

where $n_{\rm CO}$ is the CO number density, $\overline{V} = m_{\rm g}/\rho$ is the volume of the gas particle, and $\lambda_{10} = 0.26$ cm, $T_{10} = 5.53$ K, $A_{10} = 7.2\times10^{-8}\ {\rm s^{-1}}$ are the wavelength, energy level, and the Einstein A coefficient for the CO(1–0) line, respectively.

[7] Available at https://github.com/huchiayu/AstroChemistry.jl.

[8] We do so iteratively with two iterations, which has been shown to be sufficient in Hu et al. (2021).

$f_1(T_{\rm ex}) = 3\exp(-5.53/T_{\rm ex})/\sqrt{1+(T_{\rm ex}/2.77)^2}$ is the fraction of CO in the level $J=1$ (Draine 2011). Note that f_1 only varies within a factor of 2 in the range of $3 < T_{\rm ex}/{\rm K} < 30$ where most CO exists.

2.5. Simulation Setup

The initial conditions consist of a rotating disk galaxy embedded in a dark matter halo with properties resembling the WLM galaxy, generated by the MAKEDISKGALAXY code (Springel 2005). The halo has a virial radius $R_{\rm vir} = 45$ kpc and a virial mass $M_{\rm vir} = 10^{10}\,M_\odot$, and it follows a Hernquist profile (Hernquist 1990) matching a Navarro–Frenk–White (NFW; Navarro et al. 1997) profile at small radii with the concentration parameter $c = 15$ and the spin parameter $\lambda = 0.035$. The baryonic mass fraction is 0.8%, with a stellar disk of $10^7\,M_\odot$ and a gaseous disk of $7\times10^7\,M_\odot$, both following an exponential profile with a scale length of 1 kpc. The central gas surface density is $\Sigma_{\rm gas}\sim 10\,M_\odot\,{\rm pc}^{-2}$. The stellar disk follows an exponential vertical profile with a scale height of 1 kpc. The vertical density profile of the gaseous disk is set up to maintain hydrostatic equilibrium. The initial gas temperature is set to be 10^4 K. The particle mass for gas, stars, and dark matter are $m_{\rm g} = 1\,M_\odot$, $m_* = 1\,M_\odot$, and $m_{\rm dm} = 10^3\,M_\odot$, respectively. The corresponding spatial resolution for gas is ∼0.2 pc, defined as the minimum kernel radius where the Jeans length can be resolved (Hu et al. 2021). Such a high resolution is needed in order to resolve the dense and compact cores where CO is observed in the WLM galaxy. The gravitational softening length is 0.2 pc for gas and 100 pc for the dark matter.

The metallicity is $Z' \equiv Z/Z_\odot = 0.1$ throughout the simulations. The initial dust-to-gas ratio is set to be 1% of the Milky Way value, $Z'_d \equiv Z_d/Z_{\rm d,MW} = 0.01$, motivated by observations of low-metallicity galaxies (Rémy-Ruyer et al. 2014). We adopt the Milky Way dust abundances as $Z_{\rm d,MW}({\rm C}) = 1.9\times10^{-3}$ and $Z_{\rm d,MW}({\rm Sil}) = 3.5\times10^{-3}$ (Dwek 2005) corresponding to a carbonaceous-to-silicate ratio ∼0.54 and a total dust-to-gas ratio of $Z_{\rm d,MW} = 5.4\times10^{-3}$.

Galaxy scale simulations with a setup like ours are known to undergo an artificial burst of star formation during the initial collapse, which in turn leads to overly energetic SN feedback that blows out the entire gaseous disk, substantially reducing the gas surface density. Following Hu et al. (2023), we minimize this artifact by first running a simulation without dust evolution for 100 Myr and with the SN delay time set to zero. This reduces the dynamical impact of feedback due to suppressed SN clustering. The simulation snapshot at the end of this *pre-simulation* is used as the new initial conditions with a relaxed configuration.

We run three simulations: (1) a fiducial model with fully coupled chemistry and dust evolution, (2) a model without dust evolution (i.e., $Z'_d = 0.01$ throughout the simulation), and (3) a model with dust evolution where dust growth is switched off. Each simulation is run for 0.5 Gyr.

3. Results

3.1. Overview

Figure 1 shows the face-on images of the surface densities of H I, H_2, and H^+, gas temperature, projected DGR, and FUV radiation field at simulation time $t = 230$ Myr. The ISM has a complex structure, with dense clouds where star formation occurs and holes driven by stellar feedback (*SN bubbles*). The majority of gas is in the form of H I while H^+ traces the young massive stars photoionizing the ambient gas (the H II regions). The FUV radiation also traces young stars but it is more spatially extended. The H_2 abundance is extremely low everywhere besides the densest part of clouds. These paresec-scale dense cores are also where CO exists (see, e.g., Figure 3). Most of the gas is in the warm phase with a temperature of $T\sim10^4$ K, while the hot gas ($T\sim10^6$ K) is found in the interior of the SN bubbles. Cold gas with $T\sim100$ K only exists in dense and compact clouds.

The projected DGR image demonstrates that the DGR is not spatially uniform. The DGR is elevated in dense gas where dust growth is most efficient. Interestingly, the DGR is not suppressed in the interior of SN bubbles where dust is expected to be destroyed via sputtering. Instead, the DGR seems to be elevated inside the SN bubbles. Further quantitative analysis is provided in Section 3.3.

3.2. Effect on ISM Chemistry

Figure 2 shows the following global quantities of the simulated galaxy as a function of time: the H_2 mass ($M_{\rm H_2}$, top left), the SFR (top right), the luminosity of the CO(1–0) emission ($L_{\rm CO}$, bottom left), and the CO-to-H_2 conversion factor ($\alpha_{\rm CO}\equiv M_{\rm H_2}/L_{\rm CO}$, bottom right). Two simulations are shown, one with dust evolution (solid blue lines, our fiducial model) and one without dust evolution where the DGR is constant everywhere (dashed orange lines). The WLM galaxy has an observed CO luminosity of $1229\,{\rm K\,km\,s^{-1}\,pc^2}$ (Rubio et al. 2015) and an observed SFR of $1.74\times10^{-3}\,M_\odot\,{\rm yr}^{-1}$ (Hunter et al. 2010), as indicated by the red dotted lines. The CO-to-H_2 conversion factor in the Milky Way $\alpha_{\rm CO,MW} = 3.2\,M_\odot\,{\rm pc}^{-2}\,({\rm K\,km\,s^{-1}})^{-1}$ (excluding helium) is also overplotted as the red dotted line. Table 1 summarizes the median values of these global quantities.

Our fiducial model successfully reproduces the observed $L_{\rm CO}$ and SFR in the WLM galaxy. On the other hand, $M_{\rm H_2}$ is extremely low and is only a fraction of $\sim10^{-4}$ of the ISM mass. This is due to the long H_2 formation time compared to the dynamical time in the highly turbulent ISM and is consistent with previous simulations of isolated dwarf galaxies (Hu et al. 2016, 2017; Whitworth et al. 2022). The low $M_{\rm H_2}$ leads to a conversion factor close to $\alpha_{\rm CO,MW}$ despite the low metallicity. Dust evolution has a substantial impact on the CO luminosity. Without dust evolution, $L_{\rm CO}$ is about three orders of magnitude lower than the observed value. On the other hand, $M_{\rm H_2}$ and the SFR are both insensitive to dust evolution.

Our low $\alpha_{\rm CO}$ may seem to be in conflict with Hu et al. (2022) where the kiloparsec-scale $\alpha_{\rm CO}$ was found to scale with $Z'^{-0.71}$, implying $\alpha_{\rm CO}\sim5\alpha_{\rm CO,MW}$ at $Z'=0.1$. This is because we adopt $Z'_d = 0.01$ in this work (motivated by the observed superlinear metallicity–DGR relation), which is 10 times lower than what Hu et al. (2022) assumed. As a result, the molecular mass fraction $F_{\rm H_2}$ is also about 10 times lower, which explains the difference in $\alpha_{\rm CO}$.

We now take a closer look at the local chemical abundances and DGR as a function of hydrogen number density n as shown in Figure 3. The top panels show the DGR and abundances of H_2 and H I while the bottom panels show the abundances of C^+, C I, and CO. The right and left panels show models with and without dust evolution, respectively.

Dust growth enhances Z'_d only at high enough densities where $n > 10^3\,{\rm cm}^{-3}$. This is a result of the short dynamical

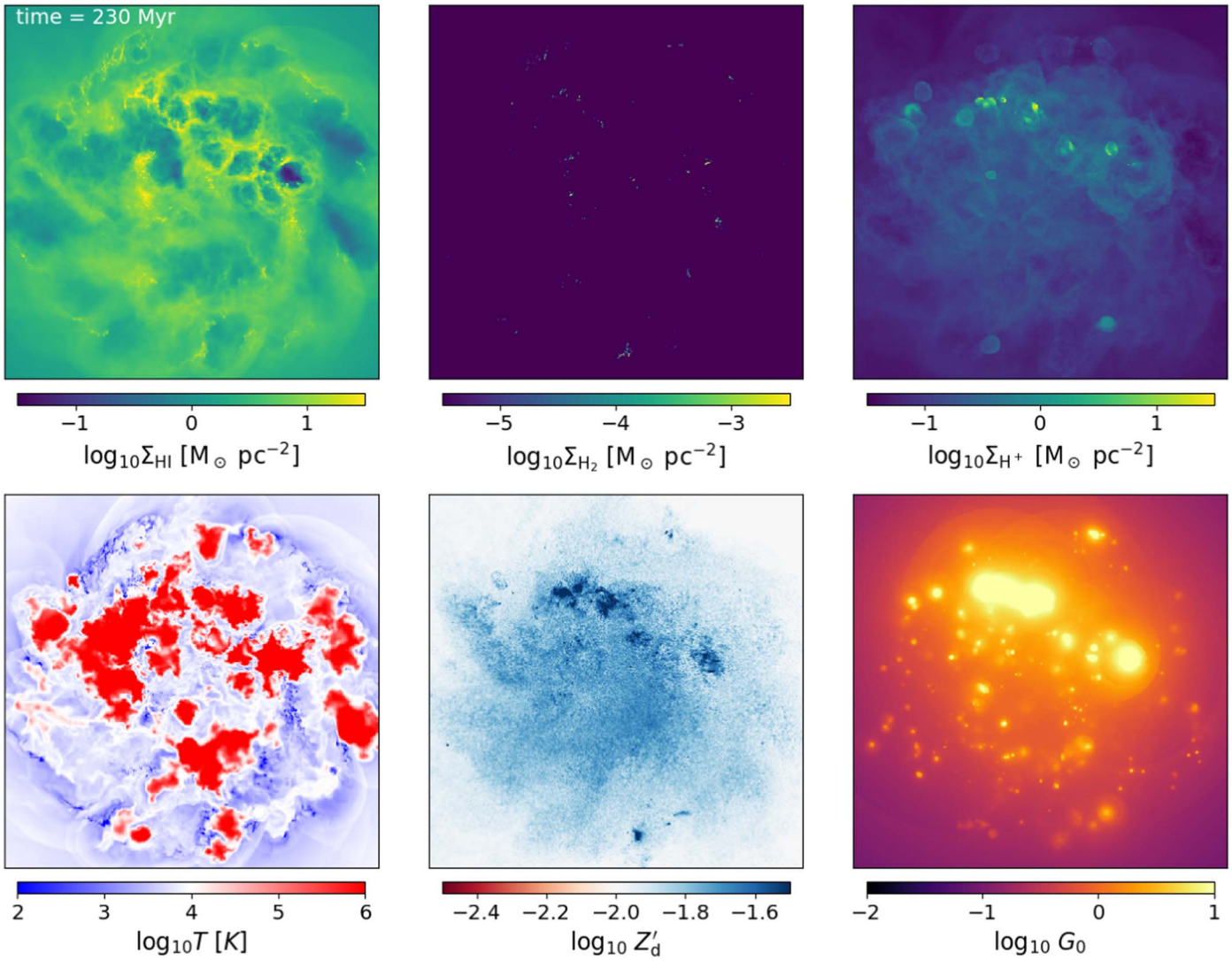

Figure 1. Face-on images of the surface densities of H I, H_2, and H^+, gas temperature (T), projected DGR ($Z_d'^{\rm proj}$), and FUV radiation field (G_0, in units of the Habing 1968 field) at simulation time $t = 230$ Myr.

time in the ISM ($t_{\rm dyn}$), which limits the available time for dust growth to operate before the dense clouds are destroyed. Indeed, the dust growth rate in Equation (4) in a static medium has the following analytic solution (Zhukovska et al. 2008):

$$f(t) = f(0)\frac{\exp(t/t_{\rm grow})}{1 - f(0) + f(0)\exp(t/t_{\rm grow})}, \quad (8)$$

where $f(0)$ is the initial dust depletion fraction and $t_{\rm grow}$ is given in Equation (6), which is density-dependent. For a given $t_{\rm dyn}$, we can therefore construct the analytic solution as a function of n, as shown in black lines in the upper right panel in Figure 3 for $t_{\rm dyn} = 0.1$ (dashed), 1 (dotted), and 10 Myr (dashed–dotted), respectively. The median Z_d' from our fiducial simulation can be reproduced remarkably well with $t_{\rm dyn} = 1$ Myr. This megayear-scale dynamical time in the ISM is consistent with that in Hu et al. (2021).

The fact that dust growth only operates at high densities ($n > 10^3\,{\rm cm}^{-3}$) means that it only modestly increases the H_2 formation rate on dust grains. Meanwhile, dust growth can also enhance radiation shielding in dense gas. However, this does not affect the H_2 abundance very much either as (1) H_2 can self-shield against the FUV radiation and (2) the limiting factor for H_2 is the available time for it to form while shielding only plays a secondary role (Glover & Mac Low 2011; Hu et al. 2021). Indeed, the H_2 abundance is only notably enhanced at $n > 10^4\,{\rm cm}^{-3}$ with dust evolution. Similarly, the SFR is insensitive to dust growth because the thermal balance of the ISM is mostly unaffected except for the densest gas.

In contrast, dust evolution has a very significant effect on the C^+/C I/CO transitions. Without dust evolution, both C I and CO are completely destroyed by the FUV radiation. This is a natural consequence of the adopted low Z_d' as motivated by observations. On the other hand, with dust evolution, C^+/C I/CO transitions take place at very high densities ($n \gtrsim 10^5\,{\rm cm}^{-3}$) due to enhanced dust shielding. This is consistent with the cloud simulations in Glover & Clark (2012b) where they found that the CO luminosity of low-metallicity clouds is dominated by emission from gravitationally collapsing dense gas of similar densities. Note that the high-Z_d' gas occupies a very small mass fraction in the ISM such that the global galaxy-integrated Z_d' is only ∼20% higher than in the constant-DGR run.

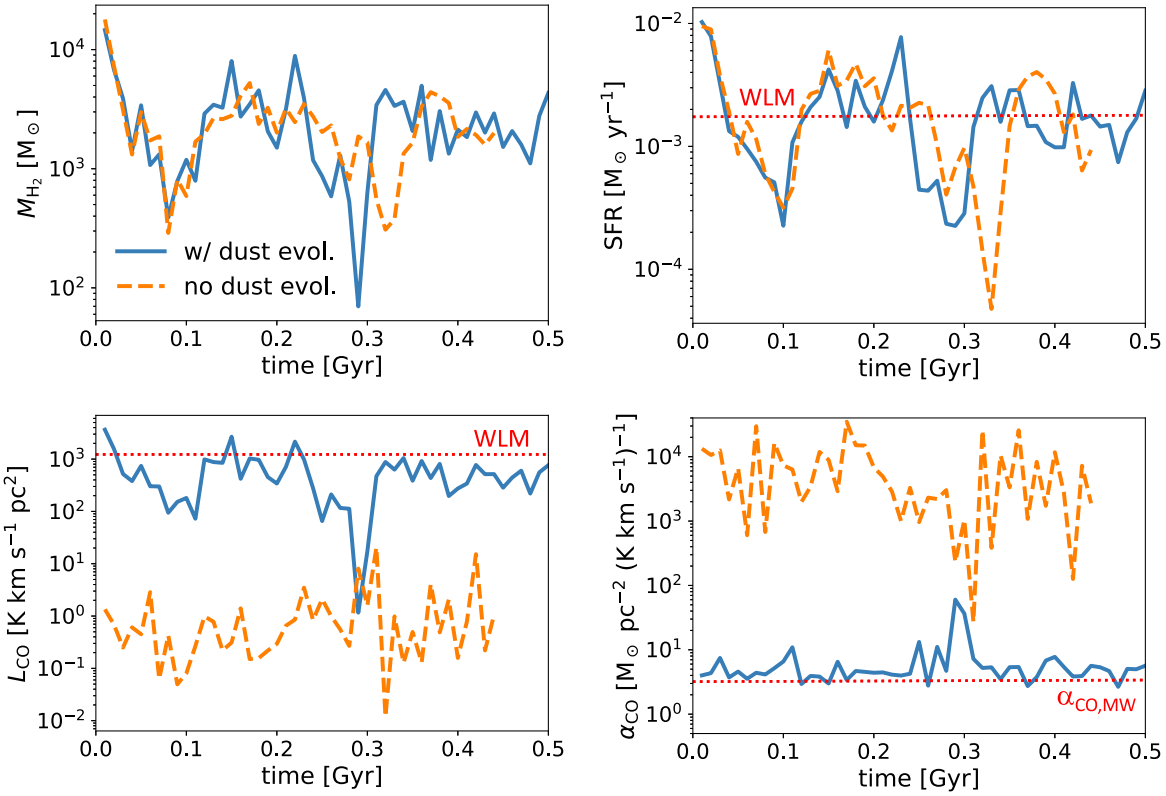

Figure 2. Time evolution of the following global properties integrated over the simulated galaxy: the H_2 mass (M_{H_2}, top left), the SFR (top right), the luminosity of the CO(1–0) emission (L_{CO}, bottom left), and the CO-to-H_2 conversion factor ($\alpha_{CO} \equiv M_{H_2}/L_{CO}$, bottom right). The solid blue lines represent our fiducial run including dust evolution while the dashed orange lines represent a controlled run without dust evolution. The red dotted lines indicate the observed L_{CO} and SFR in the WLM galaxy as well as the α_{CO} in the Milky Way. Dust evolution strongly enhances L_{CO}, but it has little effect on M_{H_2} and SFR.

Table 1
Median Values of Global Properties Over $100 < t < 500$ Myr

Model	SFR (1)	M_{H_2} (2)	M_{CO} (3)	L_{CO} (4)	α_{CO} (5)	SFR/L_{CO} (6)
With dust evolution	1.59×10^{-3}	2435	1.64×10^{-1}	469	4.63	3.41×10^{-6}
No dust evolution	2.02×10^{-3}	2095	1.97×10^{-4}	0.72	3156	2.19×10^{-3}

Note. (1) SFR [$M_\odot$ yr^{-1}]. (2) Total H_2 mass [$M_\odot$]. (3) Total CO mass [$M_\odot$]. (4) Total CO(1–0) luminosity [K km s^{-1} pc^2]. (5) CO-to-H_2 conversion factor $\alpha_{CO} \equiv M_{H_2}/L_{CO}$ [$M_\odot$ pc^{-2} (K km s^{-1})$^{-1}$]. (6) Ratio of SFR/L_{CO} [$M_\odot$ yr^{-1} pc^{-2} (K km s^{-1})$^{-1}$].

Due to the long H_2 formation time, gas with $n \sim 100\,\mathrm{cm}^{-3}$, the typical density for molecular clouds in the Milky Way, is completely dominated by H I. In other words, there is very little CO-dark H_2 gas in the ISM as often assumed at low metallicity. This leads to a galaxy-integrated α_{CO} factor only 50% higher than the Milky Way value as shown in Figure 2.

3.3. Spatial Variation of DGR

We now consider how the DGR spatial variation comes about. We compare our fiducial simulation with the simulation where dust growth is switched off to investigate the relative importance between dust growth and sputtering.

Figure 4 shows the time-averaged phase diagram (density versus temperature) color coded by Z'_d. The right and left panels illustrate the runs with (right panel) and without (left panel) dust growth. The gas distribution on the phase diagram broadly follows the classical *S-shaped* curve as determined by the thermal balance between radiative cooling and heating. Hot gas with $T > 10^5$ K is generated by SN feedback while the narrow line at $T = 10^4$ K is a signature of photoionization from massive stars.

Without dust growth, Z'_d in hot gas decreases due to sputtering. However, the highly sputtered gas (shown in red) is concentrated in the relatively high-density gas in the hot phase ($n = 0.1$–$1\,\mathrm{cm}^{-3}$), while the more diffuse hot gas is only weakly sputtered. This results from the density dependence in the sputtering rate (see Equation (3)). There is a line of red points at the lowest temperatures ($\lesssim$30 K) whose origin is still unclear. Nonthermal sputtering only operates when the dust-gas relative velocity is above 30 km s^{-1}, which is unlikely for the cold gas. We interpret this as gas particles whose associated dust was destroyed in SN shocks at an earlier time cool down to lower temperatures due to reduced photoelectric heating.

The situation becomes quite different if dust growth is included. First, as already shown in Figure 3, Z'_d in high-density gas ($n > 10^3\,\mathrm{cm}^{-3}$) is strongly enhanced as this is the place where dust growth occurs. Furthermore, Z'_d in the hot gas is slightly enhanced except for the densest and hottest region where sputtering is most efficient. This indicates that the

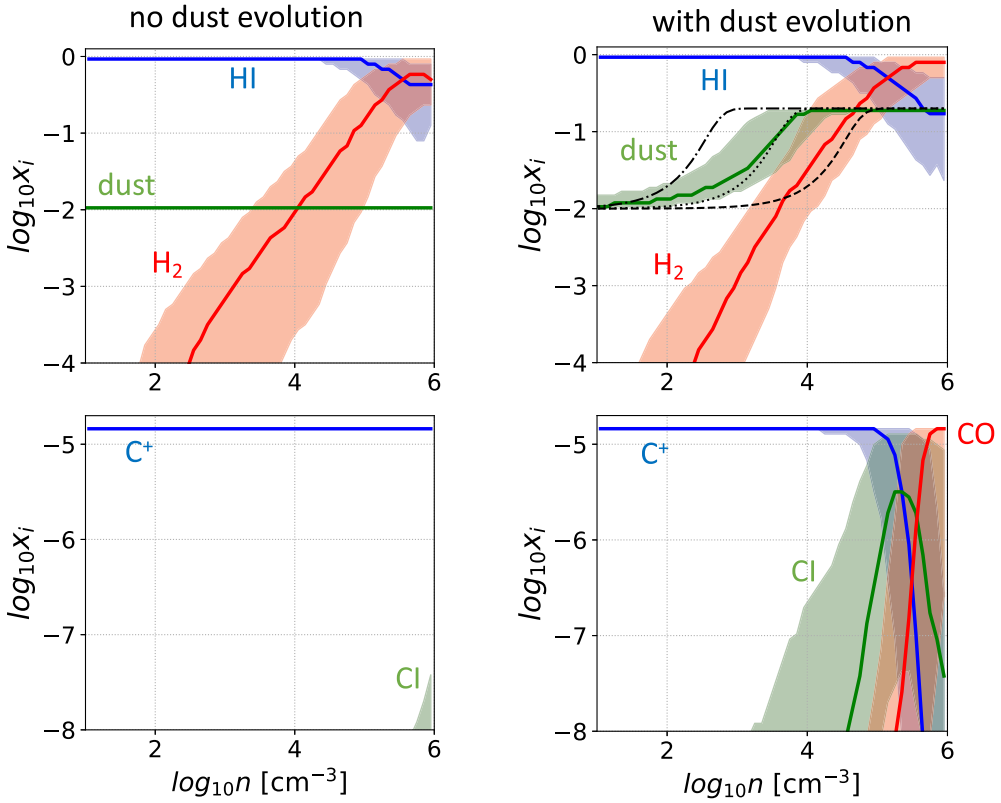

Figure 3. Top panels: the DGR normalized to the Milky Way value Z_d' (green) and chemical abundances of H I (blue) and H_2 (red) as a function of the hydrogen number density n. Bottom panels: chemical abundances of C^+ (blue), C I (green), and CO (red) as a function of n. The right and left panels are the runs with and without dust evolution, respectively. The solid lines show the median value in a given n bin while the shaded area brackets the 16th and 84 percentiles. The black lines in the upper right panel indicate the analytic solution in Equation (4) with the dynamical time $t_{\rm dyn} = 0.1$ (dashed), 1 (dotted), and 10 Myr (dashed–dotted), respectively. Without dust evolution, CO is completely photodissociated due to insufficient shielding while H_2 is almost unaffected.

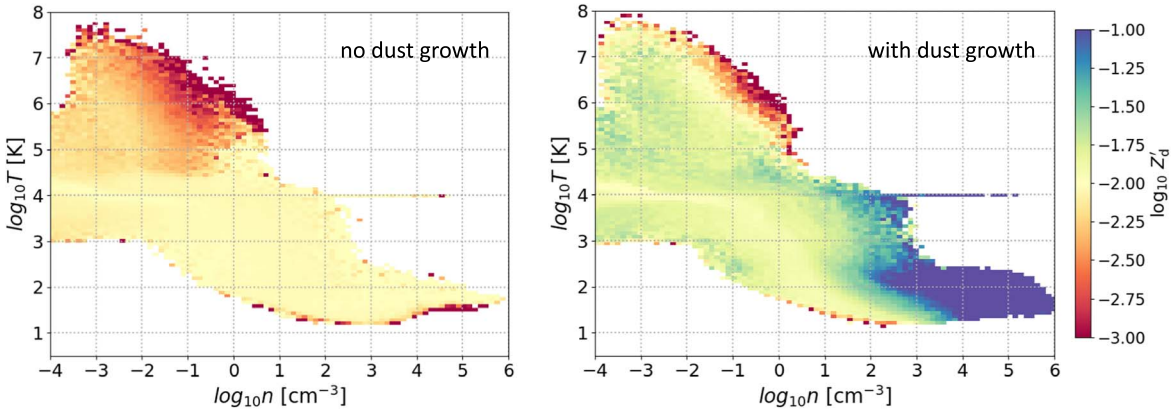

Figure 4. The time-averaged phase diagram (density vs. temperature) color coded by the DGR. The right and left panels illustrate the runs with and without dust growth, respectively. Dust growth enhances the DGR in dense gas, which mixes with the hot gas generated by SN feedback.

high-Z_d' dense gas where star formation occurs is dispersed by the subsequent stellar feedback and mixes with the ISM. As sputtering only slightly decreases Z_d', the net effect is that the hot gas is *dust-enriched*. This is qualitatively similar to metal enrichment in supernova remnants, where the SN ejecta of high metallicity mix with the ISM and increase its metallicity.

Observationally, it is more straightforward to measure the projected DGR $Z_{\rm d,proj} = \Sigma_d/\Sigma_{\rm g}$ rather than the local Z_d'. Figure 5 shows the normalized projected DGR $Z'_{\rm d,proj} \equiv Z_{\rm d,proj}/Z_{\rm d,MW}$ as a function of the gas surface density ($\Sigma_{\rm g}$) with a pixel size $l_{\rm p} = 3$ pc for our fiducial model (blue solid line) and the model without dust growth (orange dashed line).

Without dust growth, the projected DGR is fairly homogeneous everywhere. Even in the SN bubbles ($\Sigma_{\rm g} \lesssim 1\,M_\odot\,{\rm pc}^{-2}$) where sputtering occurs, $Z_d'^{\rm proj}$ is only 20% lower. Therefore, sputtering alone is insufficient to generate DGR variation. If dust growth is included, we see significant DGR variation which can be broadly divided into three regimes: (1) the compact gas clumps ($\Sigma_{\rm g} \gtrsim 100\,M_\odot\,{\rm pc}^{-2}$) where $Z_d'^{\rm proj}$ increases sharply with $\Sigma_{\rm g}$ as a direct consequence of the density-dependent dust growth, (2) the diffuse ISM ($\Sigma_{\rm g} \approx 1$–$100\,M_\odot\,{\rm pc}^{-2}$) where $Z_d'^{\rm proj}$ increases slowly with $\Sigma_{\rm g}$, reflecting the large-scale DGR variation (e.g., radial gradient) as the high-DGR gas clumps mix with the diffuse ISM, and (3)

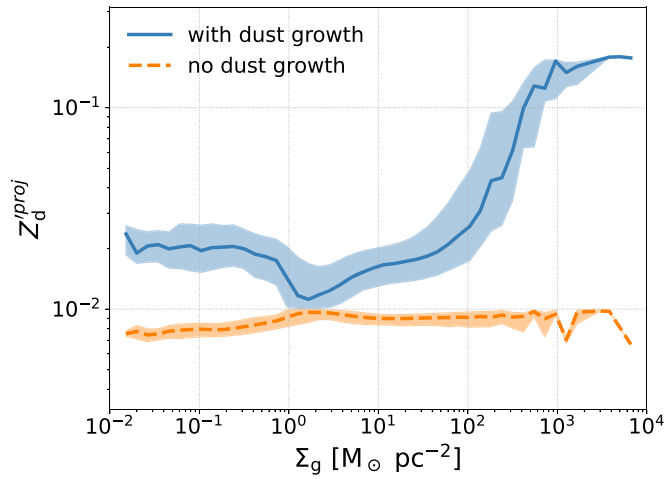

Figure 5. The time-averaged projected DGR as a function of the gas surface density with a pixel size of 3 pc. The blue solid line shows our fiducial model while the orange dashed line shows the model without dust growth. The lines show the median in each bin while the shaded area brackets the 16th and 84th percentiles. Dust growth is the main driver of the DGR variation in the ISM.

the SN bubbles ($\Sigma_{\rm g} \lesssim 1\,M_\odot\,{\rm pc}^{-2}$) where $Z_d^{\prime \rm proj}$ is enhanced by roughly a factor of two.

3.3.1. Dust in Galactic Outflows

Observations suggest that dust exists in the intergalactic medium far away from galaxies (Ménard et al. 2010; Peek et al. 2015). In this section, we quantify the SN-driven outflow rates from our simulated galaxy.

We define the mass outflow rate for gas as

$$\dot{M}_{\rm g}^{\rm out} = \int_S \rho \boldsymbol{v} \cdot \hat{n} dA, \tag{9}$$

where ρ is the gas density, $\boldsymbol{v}$ is the gas velocity, $\hat{n}$ is the outward unit normal vector of the area dA, and S is the surface where we measure the outflow rate. Similarly, the mass outflow rate for dust is defined as

$$\dot{M}_d^{\rm out} = \int_S Z_d \rho \boldsymbol{v} \cdot \hat{n} dA. \tag{10}$$

In this work, we measure the outflow rates at $|z| = z_{\rm out}$ kpc parallel to the midplane of the galactic disk. We adopt two choices of $z_{\rm out}$: 1 and 10 kpc. Following Hu (2019), the discretized outflow rate for gas and dust can be expressed as

$$\dot{M}_{\rm g}^{\rm out} = \sum_{(zv_z)_i>0} \frac{(m_{\rm g} v_z)_i}{dz}, \tag{11}$$

$$\dot{M}_d^{\rm out} = \sum_{(zv_z)_i>0} \frac{(m_{\rm g} v_z Z_d)_i}{dz}, \tag{12}$$

where the subscript i represents the particle index, v_z is the gas velocity in the vertical direction, and $dz = 0.1 z_{\rm out}$ is the thickness of the measuring plane. The summation is over particles with $zv_z > 0$ (i.e., outflowing gas) within $z = z_{\rm out} \pm 0.5\ dz$ and $z = -z_{\rm out} \pm 0.5\ dz$.

We define the mass loading factor as

$$\eta_{\rm m}(t) \equiv \frac{\dot{M}_{\rm g}^{\rm out}(t)}{\overline{\rm SFR}}, \tag{13}$$

where $\overline{\rm SFR}$ is the time-averaged SFR over the entire simulation (500 Myr). We take the averaged SFR instead of the instantaneous SFR for normalization as there is a time delay between the star formation events and the associated outflowing gas arriving at the measuring planes. Given the burstiness of the SFR, if we took the instantaneous SFR for normalization, $\eta_{\rm m}$ can be misleadingly high when the outflow rate is modest but the SFR is very low.

To quantify whether dust is preferentially expelled out of the galaxy, we define the *dust enrichment factor*

$$y_d(t) \equiv \frac{\dot{M}_d^{\rm out}(t)}{\dot{M}_{\rm g}^{\rm out}(t) Z_d^{\rm ISM}(t)}, \tag{14}$$

where $Z_d^{\rm ISM}$ is the DGR in the ISM defined as $|z| < 0.5$ kpc. Here we take the instantaneous DGR in the ISM, $Z_d^{\rm ISM}(t)$, for normalization. This is because, in contrast to the SFR, the DGR in the ISM varies very slowly over time. Note that the ratio $\dot{M}_d^{\rm out}/\dot{M}_{\rm g}^{\rm out}$ is essentially the DGR of outflows weighted by the mass flux ($m_{\rm g} v_z$).

Figure 6 shows the time evolution of $\eta_{\rm m}$ (left panels) and y_d (right panels) measured at $|z| = 1$ kpc (top panels) and $|z| = 10$ kpc (bottom panels). The blue solid line shows our fiducial model while the orange dashed line shows the model without dust growth.

We first discuss the strength of outflows. At $|z| = 1$ kpc, $\eta_{\rm m}$ fluctuates strongly with time between 1 and 30 as a result of the bursty star formation and SN feedback. At $|z| = 10$ kpc, it drops by an order of magnitude to $\eta_{\rm m} = 0.3$–1, suggesting that a large fraction of outflows measured at $|z| = 1$ kpc is balanced by inflowing gas that falls back to the disk (i.e., fountain flows), which is consistent with the findings in Hu (2019). Dust growth has a negligible effect on $\eta_{\rm m}$ as it does not affect the thermal balance and the dynamics in the ISM significantly. The difference between the two models is likely due to the intrinsic stochasticity of star formation and feedback.

We now examine the dust content in outflows. Without dust growth, the dust enrichment factor is less than unity: $y_d \sim 0.8$. This is because dust is sputtered in the shocked-heated gas in supernova remnants (SNRs: see Figure 4) that is then launched as outflows. Sputtering only destroys ~20% of dust even when the outflows have traveled to $|z| = 10$ kpc. The slightly lower y_d at $|z| = 1$ kpc does not mean that dust is created during its journey from $|z| = 1$ kpc to $|z| = 10$ kpc, which is unlikely given the low gas densities. Instead, it is likely due to dilution by the entrained ISM, which has $Z_d = Z_d^{\rm ISM}$ by definition and is expected to fall back as fountain flows rather than travel to $|z| = 10$ kpc.

The situation becomes very different once dust growth is included. The outflows are now more dusty than the ISM, with $y_d \sim 1.2$–1.5 at $|z| = 10$ kpc, as the shocked-heated gas in SNRs is *dust-enriched* due to dust growth (see Figure 4). Again, this is analogous to metal enrichment from SN ejecta, which leads to metal-enriched outflows.

3.3.2. The Effect of Beam Size

Extragalactic observations often have a telescope beam size significantly coarser than 3 pc as adopted in Figure 5. To understand the effect of beam size, we construct images of $\Sigma_{\rm g}$ and Σ_d for our fiducial model at systematically coarser beam

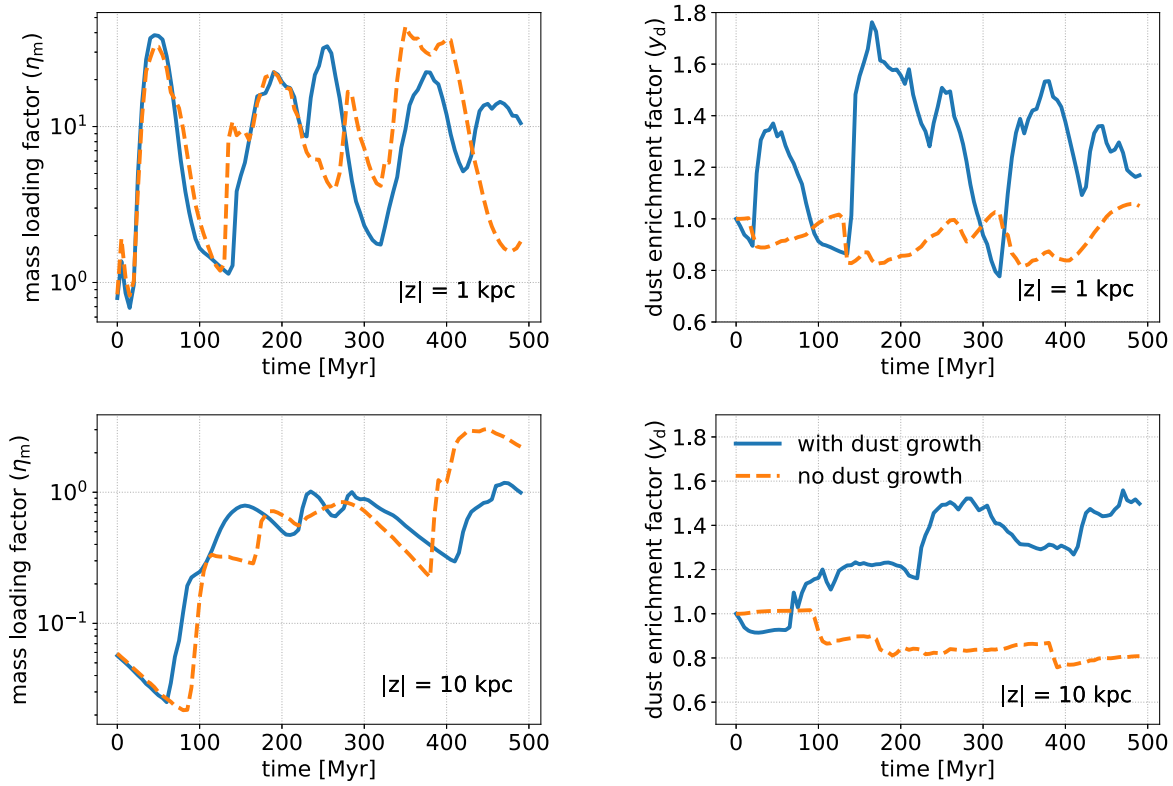

Figure 6. Time evolution of the mass loading factor (left panels) and the dust enrichment factor (right panels) of the galactic outflows measured at $|z| = 1$ kpc (top panels) and $|z| = 10$ kpc (bottom panels). Dust growth leads to dust-enriched outflows.

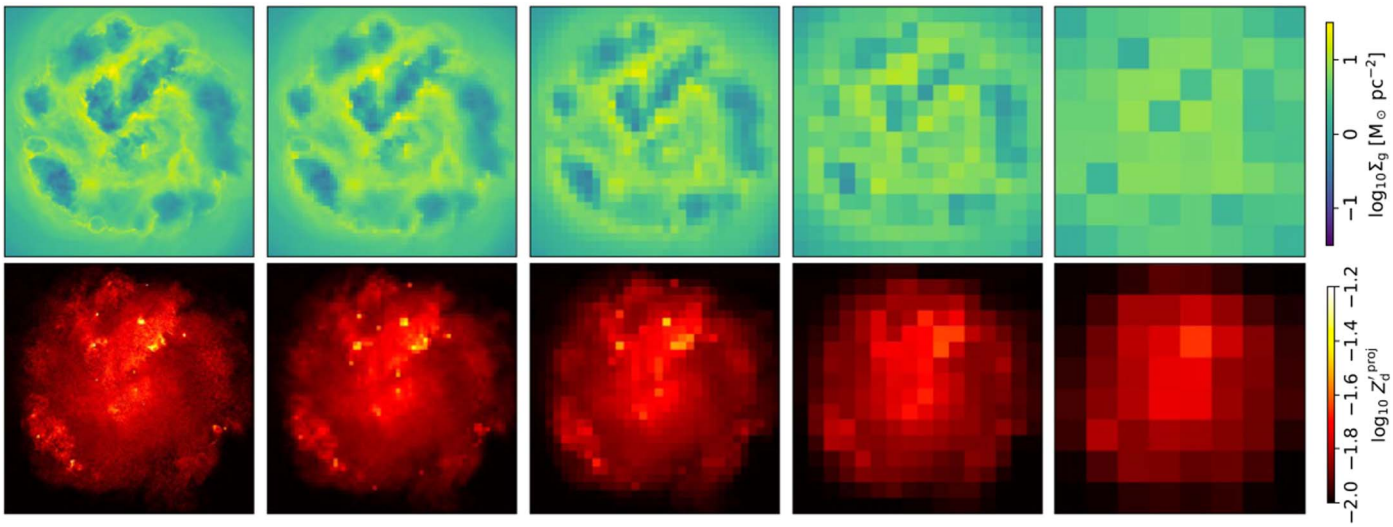

Figure 7. Images of the gas surface density (upper panels) and the projected DGR (lower panels) at $t = 240$ Myr with $l_b = 24$, 48, 96, 192, and 384 pc from left to right.

sizes of $l_b =$ 3, 6, 12, 24, 48, 96, 192, and 384 pc. For example,

$$\Sigma_g(6\text{ pc}) = \frac{\int \Sigma_g\, dA}{\int dA} = \frac{1}{2^2}\sum_{i=1}^{4} \Sigma_{g,i}(3\text{ pc}), \tag{15}$$

$$\Sigma_d(6\text{ pc}) = \frac{\int \Sigma_d\, dA}{\int dA} = \frac{1}{2^2}\sum_{i=1}^{4} \Sigma_{d,i}(3\text{ pc}), \tag{16}$$

and correspondingly,

$$Z_d'^{\text{proj}}(6\text{ pc}) = \frac{\Sigma_d(6\text{ pc})}{\Sigma_g(6\text{ pc}) Z_{d,MW}}. \tag{17}$$

Figure 7 shows the coarsened images of Σ_g (upper panels) and $Z_d'^{\text{proj}}$ (lower panels) at $t = 240$ Myr with $l_b = 24$, 48, 96, 192, and 384 pc from left to right. The compact dense gas with very high Z_d' can be resolved reasonably well at $l_b = 24$ pc. As l_b increases, this high-Z_d' gas is gradually smoothed out and the

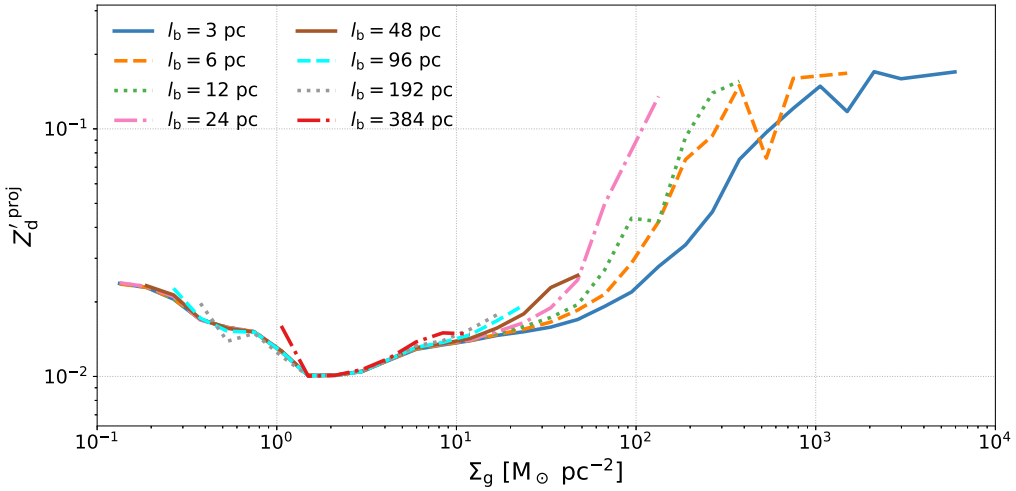

Figure 8. Same as Figure 5 but only for the fiducial model and with systematically coarser beam sizes (l_b). The scatters are not shown for clarity. Beam averaging shifts the relationship to lower gas surface densities as it smooths out the high-DGR dense gas.

DGR is significantly diluted by the diffuse ISM, which has a much lower DGR. At $l_b = 384$ pc, $Z_d'^{\rm proj}$ becomes very uniform. There is a slight radial gradient of $Z_d'^{\rm proj}$, which reflects the large-scale radial distribution of the gas surface density, similar to the metallicity gradient in galaxies caused by metal enrichment.

To be more quantitative, Figure 8 shows the relationship between Σ_g and $Z_d'^{\rm proj}$ at various beam sizes for all snapshots between $t = 100$ and 500 Myr. As l_b increases, beam averaging smooths out the dense gas such that both Σ_g and Σ_d decrease. However, Σ_d decreases less significantly because $Z_d'^{\rm proj}$ is significantly higher at high Σ_g, shifting the relationship leftward. As a result, the gas surface density above which $Z_d'^{\rm proj}$ rises sharply decreases at larger l_b. The observational implication is that measurements of the Σ_g–$Z_d'^{\rm proj}$ relationship must be compared at a similar beam size.

At even larger beam sizes ($l_b \geqslant 92$ pc), the sharply rising part disappears completely, and the Σ_g–$Z_d'^{\rm proj}$ relationship becomes insensitive to l_b. This happens when the high-Z_d' dense gas is completely diluted away by the diffuse ISM at large enough l_b. The slowly rising part corresponds to the large-scale radial gradient of $Z_d'^{\rm proj}$ as can be seen in Figure 7.

The Σ_g–$Z_d'^{\rm proj}$ relation likely depends on the metallicity and the large-scale gas surface density. We plan to conduct simulations of SMC- and LMC-like galaxies in the future for direct comparison with high-resolution far-IR (FIR) and UV observations such as those in Roman-Duval et al. (2017, 2022).

4. Discussion

4.1. Implications for the Observationally Derived DGR

Observationally, the galaxy-integrated DGR is often estimated using

$$Z_d = \frac{M_d}{M_{\rm H_2} + M_{\rm H\,I}} = \frac{M_d}{L_{\rm CO}\alpha_{\rm CO} + M_{\rm H\,I}}, \quad (18)$$

where $M_{\rm H\,I}$ is the total H I mass from the 21 cm line and M_d is the total dust mass from the FIR continuum. A major uncertainty is in the adopted $\alpha_{\rm CO}$. As a result, Rémy-Ruyer et al. (2014) reported two versions of the metallicity–DGR relation based on two different choices of $\alpha_{\rm CO}$, one is a constant Milky Way value $\alpha_{\rm CO,MW}$ and the other is metallicity dependent, which scales as Z'^{-2}. While the latter one is more frequently adopted in the literature, our results suggest that the one based on the Milky Way conversion factor is actually more appropriate at low metallicity. In fact, the metallicity-dependent $\alpha_{\rm CO}$ strongly overestimates $M_{\rm H_2}$, which in turn underestimates Z_d.

That said, our adopted initial DGR $Z'_{\rm d,0} = 0.01$ is motivated by the metallicity–DGR relation in Rémy-Ruyer et al. (2014) that assumes $\alpha_{\rm CO} \propto Z'^{-2}$, which, as we just argued above, could be an underestimate. We rerun our fiducial model in the Appendix with $Z'_{\rm d,0} = 0.03$ and find $\alpha_{\rm CO} \sim 3\alpha_{\rm CO,MW}$.

Furthermore, our simulations showed, consistent with previous studies in Hu et al. (2016, 2017), that the molecular mass fraction is extremely small ($F_{\rm H_2} \sim 10^{-4}$) in dwarf galaxies with $Z' = 0.1$ such that $M_{\rm H_2}$ contributes negligibly to the total gas mass. This is a natural consequence of the long $\rm H_2$ formation time $t_{\rm H_2} \sim 1\,{\rm Gyr}(nZ'_d)^{-1}$. With our adopted $Z'_d = 0.01$, gas at $n = 100\,{\rm cm^{-2}}$ takes $t_{\rm H_2} \sim 1$ Gyr to form $\rm H_2$, which is orders of magnitude longer than the megayear-scale dynamical time in the ISM. Therefore, the $\rm H_2$ abundance is primarily limited by the dynamical time (Glover & Mac Low 2011; Hu et al. 2021). The situation remains qualitatively similar even if we adopted $Z'_d = 0.1$ (i.e., a linear metallicity–DGR relation) as shown in Hu et al. (2016) who found $F_{\rm H_2} \sim 10^{-3}$. Consequently, the DGR should be observationally estimated simply by $Z_d = M_d/M_{\rm Hi}$ at low metallicity, and the uncertainty in $\alpha_{\rm CO}$ is irrelevant.

4.2. Implications for the Intergalactic Dust

Observations of reddening suggest that dust exists in the intergalactic medium 20 kpc to several Mpc away from galaxies (Ménard et al. 2010; Peek et al. 2015), whose origin is still poorly understood. One of the possible scenarios is dust entrained in galactic outflows (Aguirre 1999; Bianchi & Ferrara 2005). Kannan et al. (2021) conducted simulations of isolated galaxies with properties similar to those of the Milky Way and LMC coupled with a dust evolution model. They found that outflows are able to entrain dust in the fountain flows that circulate around the galaxies within a few kiloparsecs. However, they found that dust cannot be expelled to the outer part of the halos, which is in contrast to our case where outflows at 10 kpc are still dust-enriched (rather than

depleted) and are expected to eventually escape the halo (Hu 2019). This might indicate that dwarf galaxies are preferable sites to pollute the intergalactic medium with dust as they have low gravitational potential wells and the lack of hot gaseous halos around them prevents further destruction via thermal sputtering. On the other hand, the difference could also arise from numerics as the resolution in Kannan et al. (2021) is $10^3\,M_\odot$, which was presumably too coarse to resolve the dense gas where dust growth is most efficient. Resolved simulations of LMC-like galaxies have recently been conducted by Steinwandel et al. (2022b), and a systematic study of outflows across a range of galaxy masses will be valuable to shed light on this topic.

4.3. Neglected Physics

Our dust evolution model does not include dust production in SN ejecta, which has been observed (Wooden et al. 1993; Indebetouw et al. 2014) and might be a major source of dust production in the early universe when there was not enough time for AGB stars to kick in. It is still an open question as to how much dust will eventually survive once the reverse shock hits back, which depends sensitively on local gas properties (Bianchi & Schneider 2007; Micelotta et al. 2016; Kirchschlager et al. 2019; Priestley et al. 2022). Including dust production in SNe is unlikely to affect the DGR in dense gas and the ISM chemistry, but it could make the shock-heated hot gas and galactic outflows even dustier.

In addition, our dust model assumes a fixed *MRN* grain-size distribution and neglects processes that can vary the grain size such as shattering and coagulation. As the timescales for sputtering and dust growth both depend linearly on grain size, the dust production/destruction rate would be affected if the actual grain-size distribution deviates significantly from MRN. In addition, the grain-size distribution may also affect the H_2 formation rate on dust as well as dust shielding (Jonkheid et al. 2006; Romano et al. 2022). Including the evolution of grain-size distribution is therefore a highly desirable extension for future work.

5. Summary

We have presented the first ISM-resolved galaxy scale simulations coupled with time-dependent hydrogen chemistry and dust evolution. Our aim is to understand the ISM chemistry and dust properties at low metallicity, a condition expected to be common for galaxies in the very early universe observed by JWST. Our simulated galaxy is similar to the WLM dwarf galaxy, which has a metallicity of 0.1 $Z_\odot$ and has detected CO(1–0) emission. We adopt a mass resolution of $1\,M_\odot$ per gas particle which corresponds to a spatial resolution of $\sim$0.2 pc to properly resolve the compact CO cores. We post-process the simulation snapshots with a detailed chemistry network to accurately model the C^+/C I/CO transitions, taking the time-dependent abundances of H_2 and H^+ from the simulations as input parameters. Our main findings can be summarized as follows.

1. Our fiducial simulation successfully reproduces both the observed SFR and CO(1–0) luminosity ($L_{\rm CO}$) in the WLM dwarf galaxy (Figure 2). $L_{\rm CO}$ can only be reproduced if dust growth in the ISM is included, otherwise dust shielding would be insufficient to protect CO from being photodissociated by FUV radiation, suppressing $L_{\rm CO}$ by more than two orders of magnitude (Figure 3).
2. The predicted total H_2 fraction is extremely low ($\sim10^{-4}$) either with or without dust evolution due to the long H_2 formation time. This leads to very little CO-dark H_2 gas and a CO-to-H_2 conversion factor (excluding helium) $\alpha_{\rm CO} = 4.63\,M_\odot\ {\rm pc}^{-2}\ ({\rm K\ km\ s}^{-1})^{-1}$, which is only slightly higher than the Milky Way value despite the low metallicity (Table 1). Observationally inferred DGR is underestimated at low metallicity if assuming a very steep metallicity-dependent $\alpha_{\rm CO}$ (Section 4.1 and the Appendix).
3. Dust growth is the primary driver of the spatial variation of DGR in the ISM. Dust growth significantly increases the DGR in cold, star-forming clouds. Subsequent SN feedback disperses the high-DGR gas without significantly destroying the dust, leading to elevated DGR in the diffuse gas associated with supernova remnants, qualitatively similar to metal enrichment (Figures 4 and 5). As a result, galactic outflows are about 20%–50% dustier than the ISM (Figure 6). Dwarf galaxies therefore could be a source of the intergalactic dust (Section 4.2).
4. The projected DGR increases with gas surface density due to dust growth. The relationship between these two quantities varies with the telescope beam size as coarse beams smooth out the high-DGR gas clumps (Figures 7 and 8). Observational measurements should therefore be compared at a similar beam size.

Acknowledgments

We thank the anonymous referee for their constructive comments that improved our manuscript. C.Y.H. acknowledges support from the DFG via German-Israel Project Cooperation grant STE1869/2-1 GE625/17-1 and NASA ATP grant 80NSSC22K0716. A.S. thanks the Center for Computational Astrophysics (CCA) of the Flatiron Institute, and the Mathematics and Physical Science (MPS) division of the Simons Foundation for support. All simulations were run on the Raven and Cobra supercomputers at the Max Planck Computing and Data Facility (MPCDF).

Appendix
Effect of the Adopted Initial DGR

In this section, we rerun our fiducial model with an initial DGR $Z'_d = 0.03$ (instead of $Z'_d = 0.01$ as in our fiducial model) for 160 Myr.

Figure 9 shows the time evolution of $M_{\rm H_2}$, SFR, $L_{\rm CO}$, and $\alpha_{\rm CO}$ similar to Figure 2 for the fiducial model with $Z'_d = 0.01$ (blue solid) and $Z'_d = 0.03$ (orange dashed), respectively. The SFR and $L_{\rm CO}$ are very similar in both models, but $M_{\rm H_2}$ is slightly higher in the case of $Z'_d = 0.03$, leading to $\alpha_{\rm CO} \sim 3\alpha_{\rm CO,MW}$. We note that $M_{\rm H_2}$ still contributes a negligible fraction of the total gas mass ($M_{\rm H_2} \ll M_{\rm H\,I}$) and thus it can be ignored when deriving Z_d observationally with Equation (18).

Figure 10 shows Z'_d and the chemical abundances of H I, H_2, C^+, C, and CO in a similar way as in Figure 3. H_2 is more abundant in the case of $Z'_d = 0.03$ due to more efficient H_2 formation and H_2 self-shielding. On the other hand, the transition of C/CO is relatively insensitive to $Z'_d = 0.03$. This can be interpreted as dust shielding is mostly originated from the dense gas in the vicinity of the CO cores where the DGR is saturated in both cases. As such, the 3 times difference in Z'_d in the diffuse ISM has a negligible effect on the C/CO transition, which explains the similar $L_{\rm CO}$ in both models.

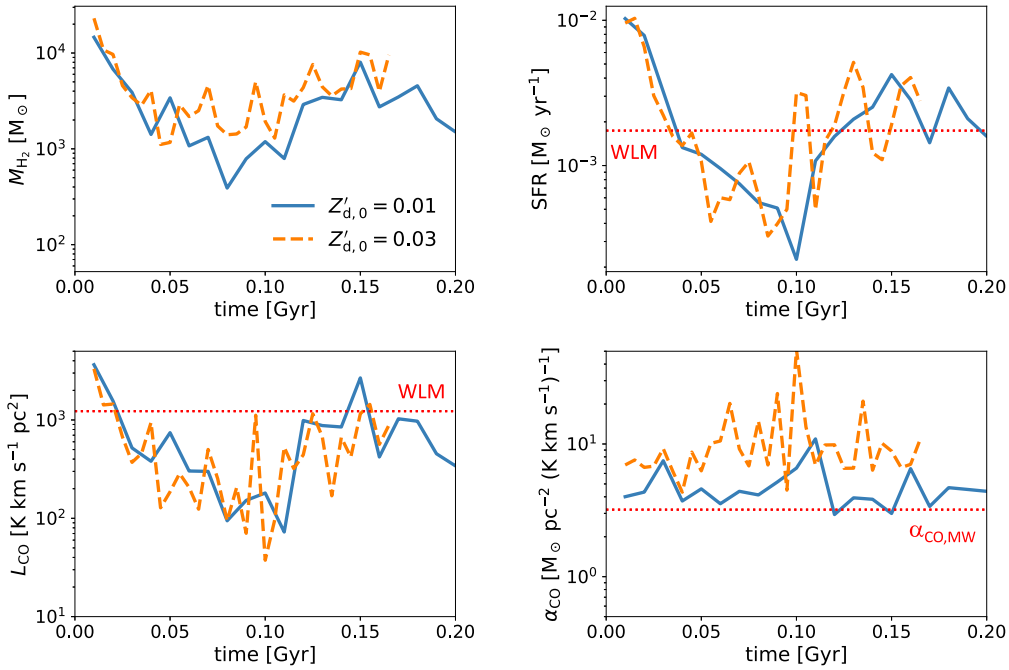

Figure 9. Same as Figure 2, but comparing models with different initial DGR: $Z'_d = 0.01$ (blue solid) vs. $Z'_d = 0.03$ (orange dashed).

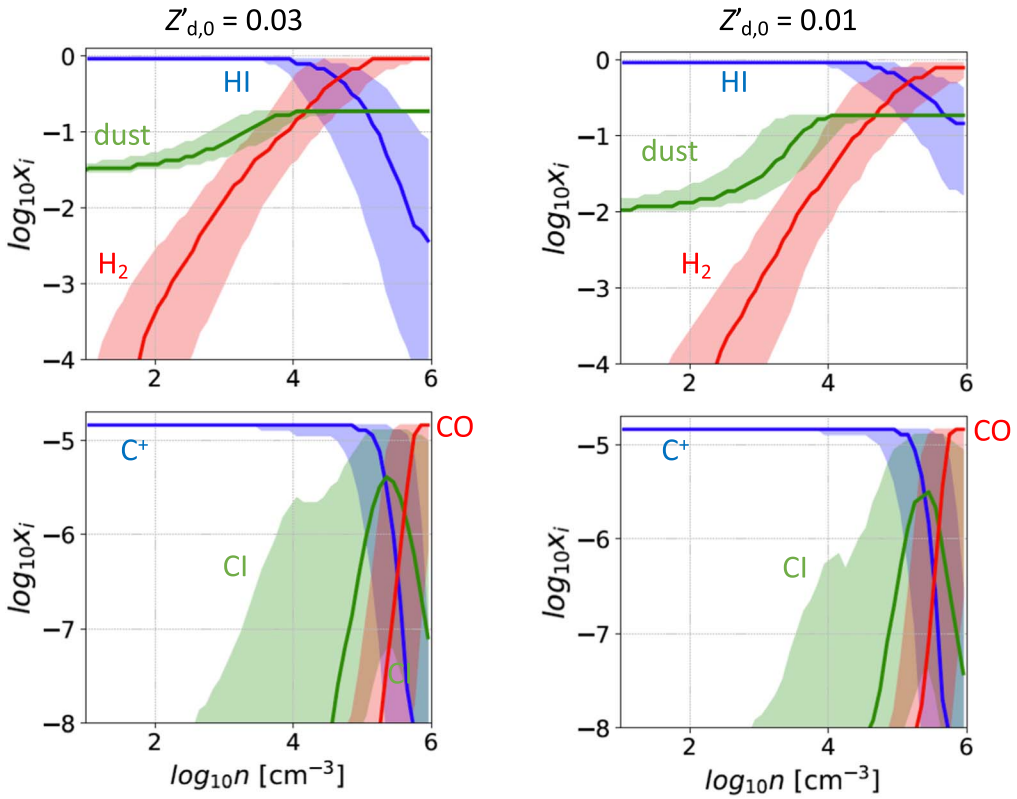

Figure 10. Same as Figure 3, but comparing models with different initial DGR: $Z'_d = 0.03$. vs. $Z'_d = 0.01$.

ORCID iDs

Chia-Yu Hu (胡家瑜) https://orcid.org/0000-0002-9235-3529
Amiel Sternberg https://orcid.org/0000-0001-5065-9530
Ewine F. van Dishoeck https://orcid.org/0000-0001-7591-1907

References

Aguirre, A. 1999, ApJ, 525, 583
Aoyama, S., Hou, K.-C., Hirashita, H., Nagamine, K., & Shimizu, I. 2018, MNRAS, 478, 4905
Aoyama, S., Hou, K.-C., Shimizu, I., et al. 2017, MNRAS, 466, 105
Bianchi, S., & Ferrara, A. 2005, MNRAS, 358, 379
Bianchi, S., & Schneider, R. 2007, MNRAS, 378, 973

Clark, P. C., Glover, S. C. O., & Klessen, R. S. 2012, MNRAS, 420, 745
Curtis-Lake, E., Carniani, S., Cameron, A., et al. 2023, NatAs, 7, 622
De Vis, P., Jones, A., Viaene, S., et al. 2019, A&A, 623, A5
Draine, B. T. 2011, Physics of the Interstellar and Intergalactic Medium (Princeton: Princeton Univ. Press)
Draine, B. T., & Bertoldi, F. 1996, ApJ, 468, 269
Dwek, E. 2005, in AIP Conf. Ser. 761, The Spectral Energy Distributions of Gas-Rich Galaxies: Confronting Models with Data, ed. C. C. Popescu & R. J. Tuffs (Melville, NY: AIP), 103
Ekström, S., Georgy, C., Eggenberger, P., et al. 2012, A&A, 537, A146
Emerick, A., Bryan, G. L., & Mac Low, M.-M. 2019, MNRAS, 482, 1304
Gaburov, E., & Nitadori, K. 2011, MNRAS, 414, 129
Glover, S. C. O., & Clark, P. C. 2012a, MNRAS, 421, 116
Glover, S. C. O., & Clark, P. C. 2012b, MNRAS, 426, 377
Glover, S. C. O., & Mac Low, M.-M. 2007, ApJS, 169, 239
Glover, S. C. O., & Mac Low, M.-M. 2011, MNRAS, 412, 337
Gong, M., Ostriker, E. C., & Kim, C.-G. 2018, ApJ, 858, 16
Górski, K. M., & Hivon, E. 2011, HEALPix: Hierarchical Equal Area isoLatitude Pixelization of a sphere, Astrophysics Source Code Library, ascl:1107.018
Habing, H. J. 1968, BAN, 19, 421
Henning, T., Jäger, C., Rouillé, G., Fulvio, D., & Krasnokutski, S. A. 2018, in IAU Symp. 332, Astrochemistry VII: Through the Cosmos from Galaxies to Planets (Cambridge: Cambridge Univ. Press), 312
Hernquist, L. 1990, ApJ, 356, 359
Hislop, J. M., Naab, T., Steinwandel, U. P., et al. 2022, MNRAS, 509, 5938
Hopkins, P. F. 2015, MNRAS, 450, 53
Hu, C.-Y. 2019, MNRAS, 483, 3363
Hu, C.-Y., Naab, T., Glover, S. C. O., Walch, S., & Clark, P. C. 2017, MNRAS, 471, 2151
Hu, C.-Y., Naab, T., Walch, S., Glover, S. C. O., & Clark, P. C. 2016, MNRAS, 458, 3528
Hu, C.-Y., Schruba, A., Sternberg, A., & van Dishoeck, E. F. 2022, ApJ, 931, 28
Hu, C.-Y., Smith, M. C., Teyssier, R., et al. 2023, ApJ, 950, 132
Hu, C.-Y., Sternberg, A., & van Dishoeck, E. F. 2021, ApJ, 920, 44
Hu, C.-Y., Zhukovska, S., Somerville, R. S., & Naab, T. 2019, MNRAS, 487, 3252
Hunter, D. A., Elmegreen, B. G., & Ludka, B. C. 2010, AJ, 139, 447
Indebetouw, R., Matsuura, M., Dwek, E., et al. 2014, ApJL, 782, L2
Indriolo, N., Neufeld, D. A., Gerin, M., et al. 2015, ApJ, 800, 40
Jonkheid, B., Kamp, I., Augereau, J. C., & van Dishoeck, E. F. 2006, A&A, 453, 163
Kannan, R., Vogelsberger, M., Marinacci, F., et al. 2021, MNRAS, 503, 336
Katz, H., Liu, S., Kimm, T., et al. 2022, arXiv:2211.04626
Kirchschlager, F., Schmidt, F. D., Barlow, M. J., et al. 2019, MNRAS, 489, 4465
Krasnokutski, S. A., Rouillé, G., Jäger, C., et al. 2014, ApJ, 782, 15
Kroupa, P. 2001, MNRAS, 322, 231
Lahén, N., Naab, T., Johansson, P. H., et al. 2020, ApJ, 891, 2
Lahén, N., Naab, T., Kauffmann, G., et al. 2023, MNRAS, 522, 3092
Lejeune, T., Cuisinier, F., & Buser, R. 1997, A&AS, 125, 229
Lejeune, T., Cuisinier, F., & Buser, R. 1998, A&AS, 130, 65
Leroy, A., Bolatto, A. D., Simon, J. D., & Blitz, L. 2005, ApJ, 625, 763
Lewis, J. S. W., Ocvirk, P., Dubois, Y., et al. 2022, MNRAS, 519, 5987
Li, Q., Narayanan, D., & Davé, R. 2019, MNRAS, 490, 1425
Lower, S., Narayanan, D., Li, Q., & Davé, R. 2023, ApJ, 950, 94
Madden, S. C., Cormier, D., Hony, S., et al. 2020, A&A, 643, A141
Mathis, J. S., Rumpl, W., & Nordsieck, K. H. 1977, ApJ, 217, 425
McElroy, D., Walsh, C., Markwick, A. J., et al. 2013, A&A, 550, A36
McKinnon, R., Torrey, P., Vogelsberger, M., Hayward, C. C., & Marinacci, F. 2017, MNRAS, 468, 1505
McKinnon, R., Vogelsberger, M., Torrey, P., Marinacci, F., & Kannan, R. 2018, MNRAS, 478, 2851
Ménard, B., Scranton, R., Fukugita, M., & Richards, G. 2010, MNRAS, 405, 1025
Micelotta, E. R., Dwek, E., & Slavin, J. D. 2016, A&A, 590, A65
Naab, T., & Ostriker, J. P. 2017, ARA&A, 55, 59
Navarro, J. F., Frenk, C. S., & White, S. D. M. 1997, ApJ, 490, 493
Nozawa, T., Kozasa, T., & Habe, A. 2006, ApJ, 648, 435
Parente, M., Ragone-Figueroa, C., Granato, G. L., et al. 2022, MNRAS, 515, 2053
Peek, J. E. G., Ménard, B., & Corrales, L. 2015, ApJ, 813, 7
Priestley, F. D., Chawner, H., Barlow, M. J., et al. 2022, MNRAS, 516, 2314
Priestley, F. D., De Looze, I., & Barlow, M. J. 2021, MNRAS, 502, 2438
Rémy-Ruyer, A., Madden, S. C., Galliano, F., et al. 2014, A&A, 563, A31
Roman-Duval, J., Bot, C., Chastenet, J., & Gordon, K. 2017, ApJ, 841, 72
Roman-Duval, J., Jenkins, E. B., Tchernyshyov, K., et al. 2022, ApJ, 928, 90
Romano, L. E. C., Nagamine, K., & Hirashita, H. 2022, MNRAS, 514, 1461
Rouillé, G., Jäger, C., & Henning, T. 2020, ApJ, 892, 96
Rubio, M., Elmegreen, B. G., Hunter, D. A., et al. 2015, Natur, 525, 218
Schruba, A., Leroy, A. K., Walter, F., et al. 2012, AJ, 143, 138
Seifried, D., Walch, S., Girichidis, P., et al. 2017, MNRAS, 472, 4797
Somerville, R. S., & Davé, R. 2015, ARA&A, 53, 51
Springel, V. 2005, MNRAS, 364, 1105
Steinwandel, U. P., Bryan, G. L., Somerville, R. S., Hayward, C. C., & Burkhart, B. 2022a, arXiv:2205.09774
Steinwandel, U. P., Kim, C.-G., Bryan, G. L., et al. 2022b, arXiv:2212.03898
Sternberg, A., & Dalgarno, A. 1995, ApJS, 99, 565
Tacconi, L. J., Genzel, R., & Sternberg, A. 2020, ARA&A, 58, 157
Weingartner, J. C., & Draine, B. T. 1999, ApJ, 517, 292
Whitworth, D. J., Smith, R. J., Klessen, R. S., et al. 2023, MNRAS, 520, 89
Whitworth, D. J., Smith, R. J., Tress, R., et al. 2022, MNRAS, 510, 4146
Wolcott-Green, J., Haiman, Z., & Bryan, G. L. 2011, MNRAS, 418, 838
Wooden, D. H., Rank, D. M., Bregman, J. D., et al. 1993, ApJS, 88, 477
Zhukovska, S., Dobbs, C., Jenkins, E. B., & Klessen, R. S. 2016, ApJ, 831, 147
Zhukovska, S., Gail, H. P., & Trieloff, M. 2008, A&A, 479, 453
Zhukovska, S., Henning, T., & Dobbs, C. 2018, ApJ, 857, 94